


Electroconvective Instability in Water Electrolysis: An Evaluation of Electroconvective Patterns and Their Onset Features

Nakul Pande^{1,2,*}, Jeffery A. Wood³, Guido Mul², Detlef Lohse¹, Bastian T. Mei², and Dominik Krug^{1,†}

¹*Physics of Fluids, University of Twente, 7500AE Enschede, Netherlands*

²*PhotoCatalytic Synthesis, University of Twente, 7500AE Enschede, Netherlands*

³*Soft matter, Fluidics and Interfaces, University of Twente, 7500AE Enschede, Netherlands*

 (Received 21 January 2021; revised 22 June 2021; accepted 2 August 2021; published 10 September 2021)

In electrochemical systems, an understanding of the underlying transport processes is required to aid in their better design. This includes knowledge of possible near-electrode convective mixing that can enhance measured currents. Here, for a binary acidic electrolyte in contact with a platinum electrode, we provide evidence of electroconvective instability during electrocatalytic proton reduction. The current-voltage characteristics indicate that electroconvection, visualized with a fluorescent dye, drives current densities larger than the diffusion transport limit. The onset and transition times of the instability do not follow the expected inverse-square dependence on the current density, but, above a bulk-reaction-limited current density, are delayed by the water dissociation reaction, that is, the formation of H^+ and OH^- ions. The dominant size of the electroconvective patterns is also measured and found to vary with the diffusion length scale, confirming previous predictions on the size of electroconvective vortices.

DOI: [10.1103/PhysRevApplied.16.034021](https://doi.org/10.1103/PhysRevApplied.16.034021)

I. INTRODUCTION

Electrolysis is projected to be a core technology for a sustainable society [1], with applications in energy storage (lithium-ion batteries, water electrolysis), climate change mitigation (CO_2 reduction), and production of useful chemicals (selective hydrogenation, N_2 reduction to NH_3). Economical considerations typically require electrolyzers for these processes to operate at large current densities [2,3], at which mostly transport processes are rate limiting. This triggers special interest into convective phenomena as a possible driver of “overlimiting currents,” that is, beyond the diffusive ion-transport limit. In the absence of external mixing, such convection may be induced by buoyancy [4,5], but can interestingly also originate from electrohydrodynamic forces. The latter, known as electroconvection, is generally associated with the instability at ion-selective interfaces (membranes or electrodes) of the formed space-charge layer [6–8]. Electroconvection has been studied extensively on ion-exchange membranes (IEMs) in the context of water desalination [9–12], on electrodes for metal electrodeposition [13–17], and recently on inert electrodes subjected to AC voltage [18]. In particular, for electrodeposition it has been shown [13–15] that electroconvection leads to a change

in the morphology of the metal deposit and dendrite formation, which may result in short circuiting in lithium-ion batteries and has implications on their design [16]. However, the electrocatalytic processes of water electrolysis, CO_2 and N_2 reduction additionally involve nonlinear bulk reactions. Their presence is known to have a strong influence on the pH distribution [19,20] and fluid properties [5,21,22], but how this affects the electroconvective phenomenon in these important systems remains unclear.

Electrohydrodynamic patterns have been reported previously in some electrolytic systems, for example, in the electrochemiluminescence of rubrene in the nonaqueous electrolyte 1,2-dimethoxyethane [23–25]. In this case, the rubrene cations and anions, which are formed at their respective electrodes, recombine in the electrolyte and emit light, thereby making the patterns visible. These were reported by Köstlin and Schaper [23] and then by Orlik *et al.* [24] who later presented a theoretical model based on ion transport to explain their results [25]. In aqueous electrolytic systems, electrohydrodynamic patterns have been visualized previously in water electrolysis using either charged carbon nanotubes [26] or colloidal spheres [27] as tracers. By further observing patterns of oxidation on ITO electrodes in the absence of the charged colloidal spheres, Han and Grier [27] confirmed that the patterns were, in fact, formed by electroconvection. However, despite these early measurements, a systematic study

*n.pande@utwente.nl

†d.j.krug@utwente.nl

of electroconvective patterns and their dependence on the electrical forcing is still required.

In this paper we present measurements of electroconvective patterns in water electrolysis. Details on the experimental setup employed are provided in Sec. II. In Sec. III A and Sec. III B, we show the results of linear sweep voltammetric and chronopotentiometric experiments, respectively. An effective reaction-diffusion model derived in Appendix B is used to explain the experimental transition times. Finally, we summarize our findings in Sec. IV.

II. EXPERIMENTAL SETUP

A schematic of the employed setup with relevant dimensions is shown in Fig. 1(a). We use a cylindrical electrochemical cell made of Teflon with a transparent platinum working electrode and a Pt-ring mesh counter

electrode (distance between working and counter electrode ≈ 4 cm) for the measurements. The transparency of the platinum electrode is obtained by sputtering a 12-nm platinum layer (with a 3-nm chromium underlayer for better adhesion) on a 170- μm glass slide. Electrical contact to the thin-film platinum electrode is made using a platinum contact pressed onto the electrode. The electrical measurements are made with a VersaStat potentiostat using a Ag/AgCl (BasiR) reference electrode. Overall, the experimental design allows for a quasi-1D [28] and unrestricted progression of the depletion front. This is in contrast to previous measurements which were performed in thin-layer electrochemical cells [23–27] (distance between electrodes approximately 100 μm) where the interaction of overlapping concentration boundary layers and bulk-recombination reactions could make the analysis of the system complicated.

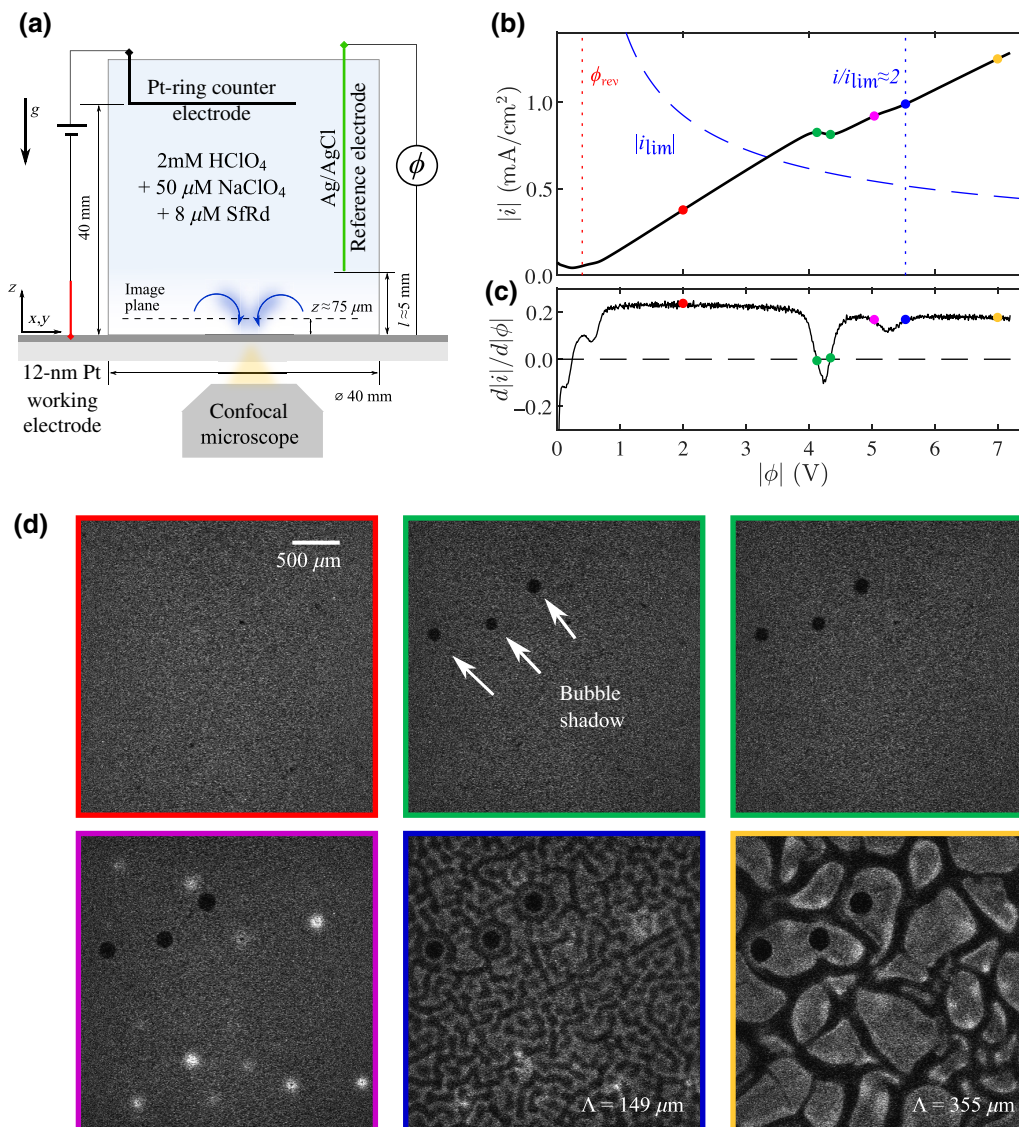


FIG. 1. (a) Schematic of the experimental setup. (b) A typical linear sweep voltammogram representative of the system response measured at a rate $|d\phi/dt| = 0.1$ V/s. The limiting current based on the Cottrell equation $i_{\text{lim}}(t)$ has been plotted as a dashed blue line. The green ($d|i|/d|\phi| = 0$), magenta and blue markers (both $d^2|i|/d|\phi|^2 = 0$) have been placed at locations of the respective transitions in $|i|$ as shown in (c). The fluorescence images in (d) are measured simultaneously with the linear sweep, and the color code corresponds to the markers in (b). The dominant wavelength, Λ , of the patterns in (d) is calculated as described in Sec. III B 3.

The electrochemical cell is mounted on an inverted laser scanning confocal fluorescent microscope (Nikon confocal microscope A1 system, Nikon Corporation, Tokyo, Japan) with a $4\times$ dry objective (CFI Plan Fluor $4\times/0.13$) which is used to measure a $3.17\text{ mm}\times 3.17\text{ mm}$ region ($512\times 512\text{ pixel}^2$) chosen close to the center of the electrode. A 561-nm excitation laser is used to excite the chosen fluorescent dye (sulforhodamine 101), whereas the emission is collected in a 545–645-nm wavelength window with a pinhole size of $28.1\text{ }\mu\text{m}$. The fluorescence measurements are made at the z -location of maximum fluorescence intensity which is $z\approx 75\text{ }\mu\text{m}$ above the electrode surface. The electrode surface is, in turn, found by the maxima of the reflected light intensity [20]. Sulforhodamine 101 (SfRd) is chosen for measurements because it is a pH- and temperature-insensitive dye [29]. A relatively small concentration of $8\text{ }\mu\text{M}$ ensured that self-quenching of its fluorescence signal, which is observed at dye concentrations approximately equal to 100 mM [30], is avoided. We further assume electrochemical stability of the dye during the (reductive) measurement. For all the measurements, the electrolyte is composed of 2 mM HClO_4 , $8\text{ }\mu\text{M}$ of SfRd, and $50\text{ }\mu\text{M}$ of supporting salt NaClO_4 . All chemicals are obtained from Sigma-Aldrich. Note that the supporting or indifferent salt affects the conductivity of the electrolyte (electrical migration effects in solution), and is purposely avoided to create conditions suitable for the onset of electroconvection. However, the application of the largest current density considered in this work (approximately equal to 10 mA/cm^2) required the addition of at least $50\text{ }\mu\text{M}$ of NaClO_4 . Nevertheless, the concentration of the supporting Na^+ ions, c_{Na^+} , is much smaller than that of the reacting H^+ ion, c_{H^+} , that is, $c_{\text{Na}^+}\ll c_{\text{H}^+}$, such that a binary electrolyte approximation can be used.

III. RESULTS AND DISCUSSION

A. Linear sweep voltammetry

We first measure the current-voltage relationship, because the onset of electroconvection at IEMs is typically associated with a characteristic shape of the current-potential curve [9,11,31]. To examine this behavior for electrocatalytic proton reduction, we sweep the potential (at a rate of $v=0.1\text{ V/s}$, starting at 0 V), as is common practice in electrochemistry [32]. The derived voltage-dependent current density, $|i(\phi)|$, is plotted in Fig. 1(b). A small decrease in $|i|$, associated with a transient capacitive current [32] (owing to sudden potential change from the open circuit potential, approximately 400 mV , to start potential of the sweep) is followed by a continuous increase up to $|\phi|\lesssim 4\text{ V}$. After an additional decrease in $|i|$, the current resumes its increasing trend with increasing $|\phi|$. This behavior is similar to that encountered on IEMs. In that case, the transient leveling off is associated with reaching the diffusion limit and the subsequent recovery of

an increasing slope in the $|i(\phi)|$ curve is linked to the driving of overlimiting currents owing to electroconvective transport [9,11]. This analogy suggests that the transition indicated by the green markers in Fig. 1(b) is related to the diffusion limit of proton reduction at the electrode surface and electroconvection setting in for $\phi>4\text{ V}$. The latter is confirmed by the results of the fluorescence imaging in Fig. 1(d). These images are measured simultaneously with the voltammogram and the corresponding times are indicated with markers of same colors in Figs. 1(b) and 1(c). Specifically, green markers are placed at $d|i|/d|\phi|=0$ and magenta and blue markers indicate points at which $d^2|i|/d|\phi|^2=0$ [see Fig. 1(c)]. Since the fluorescent dye molecules are negatively (likely single) charged [33], the lateral electric field gradients (parallel to the electrode) associated with electroconvection, that is, owing to the instability of the polarized layers near the electrode [7], initially lead to inhomogeneities in the image plane. In Fig. 1(d), initially (red marker), the dye distribution is homogeneous and in addition to the appearance of bubble shadows the image remains unchanged even as the potential is increased. At $\phi\approx 5\text{ V}$, the first inhomogeneity in the dye distribution appears (magenta marker), and eventually a very distinct pattern emerges over the entire imaged area (blue marker). At later times and even higher potentials (yellow), the typical pattern size is significantly larger, indicating an increase in size of the electroconvective vortices. The appearance of the patterns and its relation to fluid motion is likely as follows. Initially, the current at the electrode drives a depletion of ions near its surface. After significant depletion, at the onset of the instability, electric-field-driven forces appear in directions parallel to the electrode creating (1) an in-plane inhomogeneity in the fluorescent image and (2) a nonuniform electro-osmotic slip owing to its action on the space-charge layer. The resulting vortices bring in fresh fluid (rich in both positive and negative ions) from the bulk. This region of downward flow on to the electrode likely induces the bright spots in the image (as results of Davidson *et al.* [34] indicate). At the same time, the vortices also deplete the imaged plane of ions, corresponding to the dark spots at some locations in the image. Therefore, the patterns are related to the influx or efflux arm of the vortex. Ultimately, because the ions of a molecule could be thought of as migrating in cation-anion pairs, the concentration (or intensity) of the fluorescence dye should be proportional to the concentration of the background binary acid.

Determining the ratio of the measured and the limiting currents reveals to what extent the emergence of convective structures is associated with overlimiting currents. An estimate of the diffusion-limited current density can be obtained from the Cottrell equation, which holds in case the applied potential step is sufficiently large to reduce the concentration of the electroactive species (here H^+ ions) to zero at the electrode surface (i.e., in diffusion-limited

conditions) [32]. Specifically, the transient diffusion equation is solved in a semi-infinite domain with a zero concentration boundary condition at the electrode, that is, $c_{\text{H}^+}(0, t > 0) = 0$, to yield the time-dependent current density i . In the case of a binary electrolyte, this results in

$$i_{\text{lim}}(t) = -FD_s \frac{c_0}{(1 - \tau_{\text{H}^+})\sqrt{\pi D_s t}}, \quad (1)$$

where $F = 96485$ C/mol is Faraday's constant, $D_s = (2D_{\text{H}^+}D_{\text{ClO}_4^-})/(D_{\text{H}^+} + D_{\text{ClO}_4^-})$ is the effective salt diffusivity, $\tau_{\text{H}^+} = D_{\text{H}^+}/(D_{\text{H}^+} + D_{\text{ClO}_4^-})$ is the ion-transport number for the H^+ ion and c_0 the bulk concentration of the H^+ ion. Here D_{H^+} and $D_{\text{ClO}_4^-}$ are the diffusivities of the H^+ and ClO_4^- ions, respectively. We note that a zero concentration of H^+ ions at the electrode can only occur at potentials larger than the reversible potential for hydrogen evolution ϕ_{rev} (i.e., 0 V vs reversible hydrogen electrode reference; calculated to be $\phi_{\text{rev}} = -0.3972$ V for Ag/AgCl reference in Appendix 3). Therefore, Eq. (1) is applied from the time when $|\phi| \geq |\phi_{\text{rev}}|$, that is, setting $t = 0$ at the instant when $|\phi| = |\phi_{\text{rev}}|$. It is shown in Fig. 1(b) that pattern formation occurs at $i/i_{\text{lim}} \approx 2$, meaning that the pattern formation observed in Fig. 1(d) does indeed arise at overlimiting currents. A similar conclusion can be drawn from a further comparison of the current-voltage measurements with analytic expressions that take the time-dependence of the potential into account. This is presented in Appendix A where, additionally, the existence of overlimiting currents in water electrolysis at higher supporting electrolyte concentration is discussed.

Note that the analysis presented in this section does not include the role of the water bulk reaction. The treatment in this paper, moreover, does not include the second Wien effect [35], i.e., the increase in the rate of production of H^+ ions owing to an enhancement of the dissociation constant k_b for water at high electric fields [36] (for chronopotentiometric measurements, an estimate of this effect is provided in Appendix 3). It appears likely that this effect will play a role here and may be one of the reasons why electroconvection only sets in for $i/i_{\text{lim}} > 1$. Thus, there is likely an additional mechanism of enhanced dissociation rate which could provide additional reacting ions to support the increase in $|i|$ with $|\phi|$.

B. Chronopotentiometric measurements

Although voltammetric experiments are consistent with electroconvection, detailed analysis is complicated given that both i and ϕ vary in time. To correlate the onset of electroconvection to changes in the measured potential [37,38], we therefore perform experiments at constant current densities. For such configurations, the transition to electroconvection is further linked to Sand's time, that is, the time at which the electrolyte concentration vanishes

at the boundary [32]. Thus, using constant-current experiments the transition times in ϕ , the pattern onset time t_{ons} and Sand's time can be correlated.

1. Characteristic times

The potentials recorded during the constant-current experiments are presented in Fig. 2. All considered values of the current density $|i|$ are at least 100 times greater in magnitude than the steady-state diffusion-limited current density, $i_{\text{lim}} = -FD_s c_0/L = -2.89 \mu\text{A}/\text{cm}^2$, where $L = 20$ mm is half the distance between the working and counter electrode [see Fig. 1(a)]. The fluorescence images (see the Appendix, Fig. 10) confirm that pattern formation is observed in all experiments. From the potential curves, we identify two distinct times, which correspond to local minima in $d\phi/dt$ as shown in the inset of Fig. 2. From Fig. 3(a), the latter of the two times (blue square) is found to be in very good agreement with the onset time of pattern formation, t_{ons} , (obtained by visual inspection of the dye images), at all $|i|$. This connects the second (less pronounced) minimum in $d\phi/dt$ to the onset of electrokinetic instability which is therefore referred to as t_{EKI} in the following. The first minimum in $d\phi/dt$, named t_C , is not observed on IEMs [38] and is likely related to a change in the reaction at the electrode owing to transport limitations, as we show later.

Before doing so, it is useful to consider the dependence of t_{EKI} and t_C on $|i|$. First, we compare our experimental observations in Fig. 3(b) to an estimate for Sand's time given by Morris and Lingane [39], $t_{\text{ML}} = (\pi D_s)/4 (c_0 F/(1 - \tau_{\text{H}^+})i)^2$ (red line), which applies in the absence of a bulk reaction and for a binary electrolyte assuming electroneutrality. For small current densities,

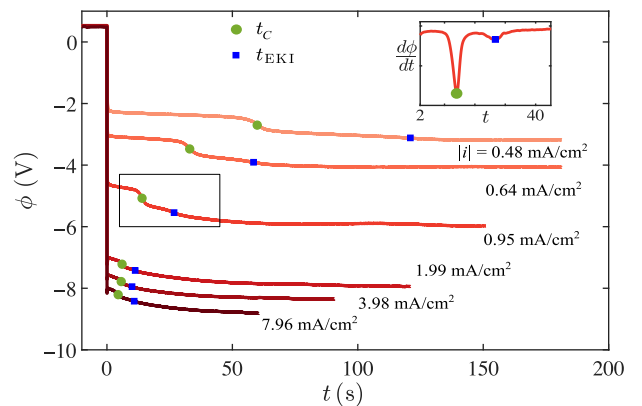


FIG. 2. Measured electrode potential (vs Ag/AgCl) at various constant-current densities $|i|$. The markers indicate locations where $d^2\phi/dt^2 = 0$ and the inset shows $d\phi/dt$ for $|i| = 0.95$ mA/cm² (corresponding to the framed box in the interval $2 \text{ s} \leq t \leq 45 \text{ s}$).

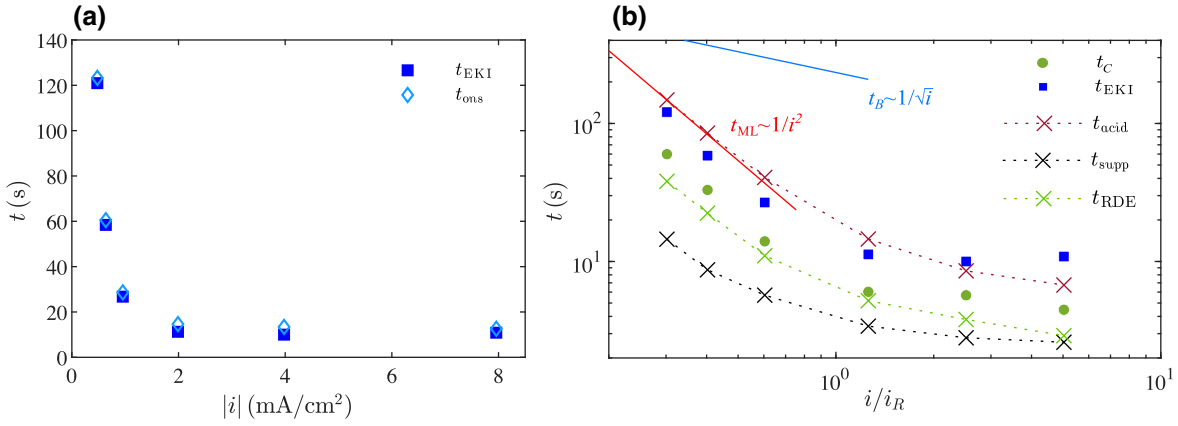


FIG. 3. (a) The onset time of the patterns from the images t_{ons} , compared to the transition time t_{EKI} measured from Fig. 2. (b) Log–log plot of the transition times t_{EKI} and t_C vs i normalized by the bulk-reaction-limited current density i_R . The error bars are smaller than the symbols. (The uncertainty in the measurement of the experimental times t_C and t_{EKI} is related to the window size of the moving average filter (50 points) that is applied to obtain $d\phi/dt$ shown in the inset of Figure 2. Therefore, the error bars are ± 0.25 s. For t_{ons} the error bars are related to the time resolution of the optical measurement, that is, ± 0.033 s.) t_{ML} is Sand’s time as defined in [39]. Here t_{acid} , t_{supp} , and t_{RDE} are transition times ($c \rightarrow 0$) discussed in the main text and obtained from numerical simulation of the reaction-diffusion system of equations defined in Appendix B. Each of these are depicted with a cross marker and provided with dotted lines to guide the eye. Here t_B is the onset time for buoyancy convection using Eq. (6). Note the convention: solid symbols indicate experimental times, the oblique cross symbols the numerical times, and the solid lines the analytical estimates.

t_{EKI} is found to be in good agreement with t_{ML} . Moreover, both t_C and t_{EKI} follow the classical $1/i^2$ relationship implied by the expression for t_{ML} . With increasing $|i|$, however, the decrease of t_C and t_{EKI} is significantly slower. In fact, we find that the deviation occurs around a “bulk-reaction-limited” current density i_R , which reflects the maximum current (or proton flux) that can be sustained at the electrode by the bulk-reaction term when the concentration at the electrode reaches diffusion limitation. In particular, $i_R = -FD_{\text{H}^+c_0}/\delta_R = -Fk_b c_W \delta_R$, where $\delta_R = \sqrt{D_{\text{H}^+c_0}/k_b c_W}$ is the size of the reaction-diffusion boundary layer for dissociation of water, based on a balance between diffusive flux approximately $D_{\text{H}^+}(c_0)/\delta_R^2$ and production owing to water dissociation approximately $k_b c_W$, where k_b and c_W are the dissociation constant and water concentration, respectively (values of constants can be found in Appendix B).

To explore the reason for the change in scaling behavior for t_C and t_{EKI} at $i/i_R \approx 1$ [see Fig. 3(b)], we consider the ion-transport equations for the different components of the acidic electrolyte. As shown in Appendix B, assuming electroneutrality, the corresponding system of equations is reduced to a reaction-diffusion system in the limit of two extreme cases: (1) in the absence of supporting electrolyte, called “acid” henceforth, and (2) with excess supporting electrolyte (“supp”). Although in acid the transport of H^+ ions is coupled to ClO_4^- ions, in supp the H^+ ions move independently of the other ions in solution. For both cases, we integrate the transport equations numerically and obtain the respective Sand’s times, t_{acid} and t_{supp} , which are presented in Fig. 3(b). Here t_{acid} and t_{supp} provide an

envelope for both the experimental transition times, that is, $t_{\text{supp}} < t_C, t_{\text{EKI}} < t_{\text{acid}}$. Moreover, t_{acid} , which is an estimate of Sand’s time in the case of negligible supporting electrolyte, approximates t_{EKI} reasonably well. Importantly, t_{acid} approaches t_{ML} (see previous paragraph for definition) at $i/i_R \ll 1$, and differs significantly from t_{ML} for $i/i_R \gtrsim 1$, revealing the increasing importance of the bulk reaction at higher current densities, which causes the deviation from the classical scaling.

The preceding discussion shows that the time of the second (electroconvective) transition in ϕ is approximated reasonably well by Sand’s time t_{acid} . The small but distinct potential change at t_{EKI} in Fig. 2 is therefore related to the vanishing conductivity at the boundary [see Eq. (B6)]. Here, we provide a possible explanation for the additional transition at t_C in terms of a change in the reaction at the electrode at the moment when diffusion limitation, that is, $c_{\text{H}^+} \approx 0$, is encountered at the electrode surface.

To do so, we consider the kinetic boundary condition at the reaction plane which can be expressed as the generalized Frumkin-Butler-Volmer equation [40–43] for the Faradaic current (i_F) at the boundary. It reads

$$i_F = k_- c_{\text{H}^+} \Gamma (1 - \theta) e^{-\alpha \Delta \phi_S / \phi_T} - k_+ \Gamma \theta e^{\alpha \Delta \phi_S / \phi_T} \quad (2a)$$

where

$$i_F = D_{\text{H}^+} \left(\frac{\partial c_{\text{H}^+}}{\partial z} + \frac{c_{\text{H}^+}}{\phi_T} \frac{\partial \phi}{\partial z} \right) \Big|_{z=0}. \quad (2b)$$

Here, k_- is the rate constant for the reduction reaction (formation of PtH_{ads}), k_+ for the corresponding oxidation

reaction, $\alpha = 0.5$, Γ the total number of available sites for reaction, θ the fractional coverage, $\Delta\phi_S$ the potential drop across the Stern layer driving the reaction and $\phi_T = RT/F$ the thermal voltage (R is the ideal gas constant, $T = 298$ K).

We rewrite Eq. (2a) as

$$i_F = i_{\text{kin}} \left(1 - \frac{k_+ \theta}{k_- (1 - \theta) c_{\text{H}^+}} e^{2\alpha \Delta\phi_S / \phi_T} \right) \quad (3)$$

$$\text{with } i_{\text{kin}} = k_- c_{\text{H}^+} \Gamma (1 - \theta) e^{-\alpha \Delta\phi_S / \phi_T}, \quad (4)$$

where i_{kin} is the kinetic current. For fast reversible reactions, such as proton reduction on platinum, $i_F / i_{\text{kin}} \ll 1$ [44] and quasiequilibrium is maintained (right-hand side of Eq. (3a) = 0). Thus, Eq. (2a) reduces to the Nernst equation and the potential drop across the Stern layer, $\Delta\phi_S$, can be estimated using

$$\frac{\Delta\phi_S}{\phi_T} = \frac{1}{2\alpha} \ln \frac{k_- (1 - \theta) c_{\text{H}^+}}{k_+ \theta}. \quad (5)$$

Finally, it can be seen that $c_{\text{H}^+} \rightarrow 0$ is equivalent to $\theta \rightarrow 1$ at the reaction boundary, that is, a change from the underpotential to overpotential hydrogen deposition at the electrode [45].

To estimate the time of this transition from the transport equations, we heuristically assume that the potential gradient vanishes at the reaction plane, $\partial\phi/\partial z|_{z=0} = 0$, and solve the electroneutrality equations with a modified flux boundary condition at the electrode, $D_{\text{H}^+}(\partial c_{\text{H}^+})/\partial z = i/F$ [instead of Eq. (B11a)]. This is similar to the “zero-field approximation” that has been used to model electrode reactions in the absence of a supporting electrolyte for fast electron transfer reactions [46,47], but with the added simplification of electroneutrality. The zero-field approximation inherently assumes that the Stern layer adsorbs ions that screen the surface charge [43]. Since electrocatalytic proton reduction on platinum is a fast reaction and proceeds first by an (underpotential) adsorption of protons at the boundary, this approximation appears justified in the present system.

The transition time within this approximation, t_{RDE} , is the moment when the flux of protons at the electrode becomes diffusion limited, i.e., when $c(z=0) = 0$. Model results for t_{RDE} are compared with t_C in Fig. 3(b). The values are close and the small difference between the two is indeed expected since t_C corresponds to the inflection point in ϕ (inset Fig. 2) whereas t_{RDE} actually predicts the time at the base of the spike in $d\phi/dt$. Note that an overview of all time scales used is provided in Table I.

TABLE I. Summary of the characteristic times.

| Experimental measured times | | |
|-----------------------------|-------------------------------------|--|
| t_C | Critical time | First peak in $d\phi/dt = 0$ in Fig. 2, or the first time of transition in the measured electrode potential |
| t_{EKI} | Electrokinetic instability time | Second peak in $d\phi/dt = 0$ in Fig. 2, or the second time of transition in the measured electrode potential |
| t_{ons} | Pattern onset time | Time at which a peak is detected in the radially averaged fourier spectrum of the fluorescence image, i.e., $\psi > 0.15$ in Fig. 5(a) |
| Numerical times | | |
| t_{acid} | Binary acid time | Time at which $c_{\text{H}} \rightarrow 0$ for a binary acidic electrolyte with a bulk-reaction term. This serves as an estimate for the onset times of electroconvection t_{EKI} (or t_{ons}) |
| t_{supp} | Excess supporting electrolyte time | Time at which $c_{\text{H}} \rightarrow 0$ for an electrolyte with excess supporting salt (no potential drop in bulk solution) |
| t_{RDE} | Reaction-diffusion (electrode) time | Time at which $c_{\text{H}} \rightarrow 0$, based on a model that assumes a vanishing potential gradient at the reaction plane. This serves as an estimate for the measured critical time t_C and likely represents a transition from an underpotential to overpotential deposition of H^+ . |
| Analytical times | | |
| t_{ML} | Morris-Lingane time | Analytical estimate of Sand’s time for purely diffusive case (no bulk reaction) as obtained in [39] |
| t_B | Buoyancy time | Estimate for onset time for buoyancy-driven convection: the time at which the Rayleigh number (buoyancy driving) exceeds critical value of 817. See Eq. (6) |

2. Role of buoyancy

Previous studies have shown that buoyancy may influence electroconvection [38,48]. Here we briefly discuss the role of buoyancy forcing in the present system. The relevant dimensionless parameter in this context is the Rayleigh number Ra , which compares buoyancy and viscous forces. For our configuration, we define

$$Ra = \frac{g\beta d^4}{D_S\eta} \frac{\partial c}{\partial z}, \quad (6)$$

where g is the acceleration due to gravity, $d \approx \sqrt{D_S t}$ is the characteristic length scale of the gradient, and $\eta = 10^{-3}$ Pa s is the dynamic viscosity of water at 293 K. The density gradient can be estimated by using the concentration flux at the boundary $\partial c/\partial z = i(1 - \tau_{H^+})/(FD_S)$ in the electroneutrality limit [39], and the coefficient $\beta \approx \Delta\rho/\Delta c = 0.0575$ kg/mol [49] for density change with depletion of HClO_4 at the electrode. With a critical value for the onset for buoyancy-driven convection of $Ra_c = 817$ [50,51], we obtain the relation

$$it_B^2 = Ra_c F\eta / (g\beta(1 - \tau_{H^+})) \quad (7)$$

for the variation of the onset time t_B for buoyancy convection. The implied dependence $t_B \sim 1/\sqrt{i}$ is compared with the other transition times in Fig. 3(b).

Tan and Thorpe [51] have shown that the choice of the diffusion length scale (here $\sqrt{D_S t}$) may underpredict the Rayleigh number and, hence, overestimate t_B . We can check whether the estimate in Eq. (6) is accurate by redefining the Rayleigh number using the numerical concentration profiles, similar to what was done by de Valença *et al.* [38]. In Fig. 4(a), we present the time evolution of the concentration profiles c normalized with the initial/bulk concentration c_0 for the smallest applied $|i|$. The effective diffusion layer thickness $\delta_B(t)$ is taken as the distance from the boundary where $c = 0.98c_0$, and we define the Rayleigh number now based on this quasisteady length scale as

$$Ra^* = \frac{g\beta\Delta c\delta_B^3}{D_S\eta}, \quad (8)$$

where $\Delta c = c_0 - c(0, t)$ is the effective concentration depletion in the diffusion layer. The dotted line in Fig. 4(a) indicates the estimated diffusion layer for numerical concentration profiles at three representative times.

The time evolution of Ra^* at different $|i|$ is presented in Fig. 4(b). Note that we have normalized the time axis with Sand's time t_{acid} (which is an estimate of electroconvection onset time from the model) to indicate whether buoyancy-driven convection occurs before electroconvection. When $Ra^* > Ra_c$, the onset of buoyancy-driven convection is expected. From Fig. 4(b), we conclude that for

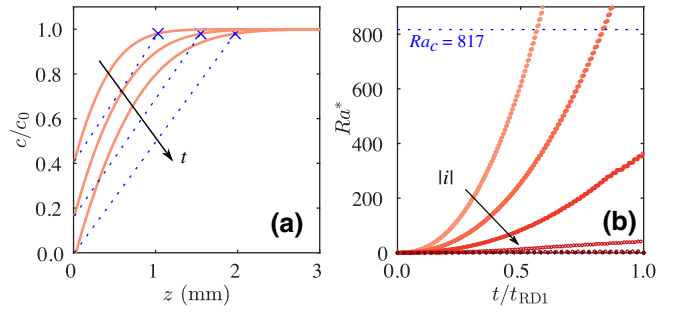


FIG. 4. (a) Solid lines: concentration profiles of HClO_4 at times $t = 51$ s, 103 s and 153 s obtained from the numerical model “acid” for the smallest current density $|i| = 0.48$ mA/cm². The dotted line shows the effective diffusion layer which is used to calculate Ra^* . (b) The evolution of the critical Ra^* for all current densities. Ra_c is an estimate of the critical Rayleigh number for the present configuration.

the lower two current densities, the onset of buoyancy mixing may be expected before electroconvection. This would explain the sudden smoothing of the pattern after its onset for the smallest current density (Fig. 10), which is most likely caused by large-scale buoyant mixing. For the rest, however, we observe that electroconvection precedes any density-driven mixing ($Ra(t_{\text{acid}}) \ll Ra_c$). It therefore appears unlikely that the different scaling of the transition times for the three largest current densities, at $i/i_R \gtrsim 1$ in Fig. 3(b), is a buoyancy effect. Nevertheless, because electroconvection can accelerate the onset of buoyancy-driven convection [48], it may drive mixing at later times.

3. Structure size and evolution

In addition to the transition times, we can also determine a typical length scale of the patterns as a measure of the size of the electroconvective vortices [10]. We find the dominant wavelength Λ of the patterns from the maximum in the radially averaged one-sided power spectrum ψ of the mean subtracted fluorescence intensity of the images. In Fig. 5(a) we present the time evolution of ψ for a particular current density $|i| = 0.95$ mA/cm². There is a clear dominant wavelength of the pattern which increases with time. At each time, Λ is taken as the vertex of the parabola (red line) that is fit to the three points adjacent to the peak.

Figure 5(b) shows that when shifted by their respective instability time t_{EKI} , the growth of Λ consistently follows a diffusive behavior with $\Lambda \approx \sqrt{D_{H^+} t}$ across all $|i|$. The similarity in the pattern evolution at different current densities is also evident from fluorescence images directly (see Appendix D). This result is in line with the numerical prediction of Rubinstein and Zaltzman [6] who showed that the size of electroconvective vortices in steady state (which evolves through the merging of smaller vortices) is equal to the length scale of the diffusion domain. The

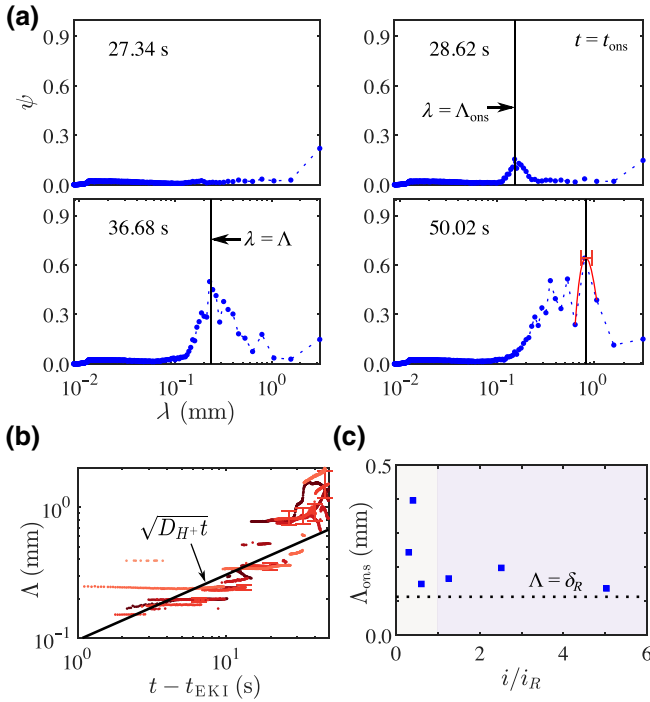


FIG. 5. (a) Radially averaged power spectrum ψ , plotted against the wavelength λ at different times for $|i| = 0.95 \text{ mA/cm}^2$. The dotted line is provided to guide the eye. A parabola (red curve) is fit around the maximum value and two adjacent points to obtain the wavelength of instability Λ . (b) The peak wavelength of the pattern Λ is plotted as a function of time, for all current densities after their onset. The color scheme is the same as used in Fig. 2. Typical error bars have been shown for a single case $|i| = 0.95 \text{ mA/cm}^2$. The solid black line shows the diffusion length scale $\sqrt{D_H t}$. (c) Structure size at onset $\Lambda(t_{\text{ons}}) = \Lambda_{\text{ons}}$ as a function of the current density, where δ_R is the size of the bulk-reaction-diffusion boundary layer.

agreement with the steady-state prediction, moreover, indicates that in our system the vortices grow in a quasisteady manner despite the transient evolution of the diffusion layer. Figure 5(b) is also consistent with measurements in IEMs [10] where a similar scaling was measured for the electroconvective vortex size (for a single membrane pore, or nanoslot), although with a time-varying electrical forcing.

Note that with $\sqrt{D_H t}$ being an estimate of the vertical propagation of the diffusive front, our findings imply a typical aspect ratio (lateral wavelength over height of the structures) of 1. Lastly, in Fig. 5(b) we plot the initial wavelength of the patterns $\Lambda_{\text{ons}} = \Lambda(t_{\text{ons}})$ (taken at the empirical threshold value $\psi = 0.15$, see Fig. 5(a) at $t \approx 29 \text{ s}$). The value of Λ_{ons} saturates at the reaction-diffusion boundary-layer thickness $\Lambda = \delta_R$ for $i/i_R > 1$, which is another manifestation of the limiting behavior observed for the pattern onset time.

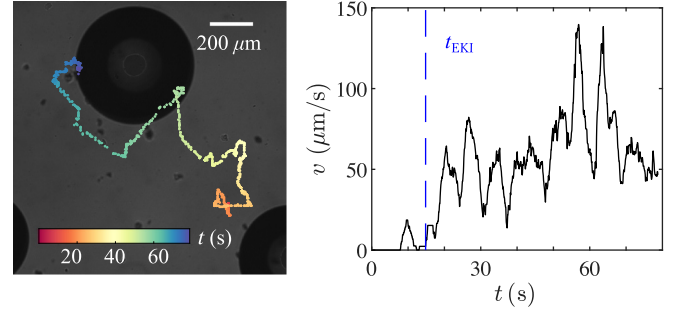


FIG. 6. Measurements for $i \approx 2.3 \text{ mA/cm}^2 = 1.5 i_R$. (a) Time trace of the motion of a particulate impurity in solution. The particle path has been overlaid on the final (backlit) image taken of the electrode. The dark circle represents the bubble shadow. (b) In-plane velocity of the particle. Here t_{EKI} has been measured from the fluorescence images. Full movie available in Supplemental Material [52]. Note that to obtain the time trace and the velocity, the particle location is determined from each image frame by visual inspection.

4. Convective motion

In addition to the dye images and the footprint in the potential curves at t_{EKI} , we also obtain direct evidence of convective motion in the fluid by tracking the motion of a particulate impurity (size $\hat{a} \approx 40 \mu\text{m}$). The time trace of motion and the in-plane velocity are shown in Fig. 6. We find that the particle, initially at rest, moves vigorously only after $t = t_{\text{EKI}}$, with velocities, $v \sim 100 \mu\text{m/s}$, comparable with electroconvective velocities measured in [38]. It should be noted that measurement with fluorescent tracer particles (Thermo Scientific, Fluoro-Max Red 36-2B, $6 \mu\text{m}$) failed, because, presumably due to electrophoretic effects, these quickly disappeared from the measurement plane once the patterns emerged. The particulate impurity is apparently charged to a lesser extent compared with the tracers. Yet it is still conceivable that also in this case the velocity $v_{\text{EP}} = \mu_p E_b$ induced by the bulk electric field E_b may be significant. To test this, we estimate the electrophoretic mobility μ_p using the relation for a spherical colloidal particle [53]: $\mu = 2\varepsilon_r \varepsilon_0 \zeta_p / 3\eta f(a/\lambda_D)$, where ε_0 is the permittivity of a vacuum, $\varepsilon_r = 80$ is the relative permittivity of water, $f(a/\lambda_D)$ is Henry's function which depends on the ratio of the particle size to the Debye layer thickness $\lambda_D = \sqrt{\varepsilon_0 \varepsilon_r RT / (2F^2 c_0)} = 6.8 \text{ nm}$ (for $\hat{a}/\lambda_D \gg 1$, $f = 1.5$) and $\zeta_p \approx 0.1 \text{ V}$ is the assumed zeta potential of the particle. We approximate E_b , based on the steady-state diffusion of counter ions as $E_b = (RT/F/c)\partial c/\partial z \approx RT/F/\delta_R = 220 \text{ V/m}$, where diffusion length is taken to be its limiting value δ_R . The electrophoretic velocity is therefore calculated to be $v_{\text{EP}} \approx 16 \mu\text{m/s}$. Although v_{EP} is smaller than the maximum particle velocity $v_{\text{max}} \approx 150 \mu\text{m/s}$, it is of the same order of magnitude as the value measured soon after pattern onset ($\approx 50 \mu\text{m/s}$). This

implies that the electrophoretic force on the particle cannot be disregarded and that an accurate measurement of the fluid velocity would require particles with well-defined zeta potentials. Nevertheless, because v_{\max} is an order of magnitude larger than v_{EP} , it is likely that there is fluid motion in the present system.

A final remark is given regarding the roles of the bubbles that can be seen to nucleate occasionally (see Fig. 1) and can cause bending of electric field lines around them (the case of a dielectric sphere in an electric field [54]). However, the presence of such a perturbation does not appear to significantly influence the transition times as evidenced by the good agreement between the experimental results and those from the one-dimensional ion-transport model. Further, the pattern formation does not necessarily initiate from bubble locations and the structures generally appear unaffected by the bubbles, except in their immediate vicinity.

IV. CONCLUSION

In summary, we investigate electroconvective pattern formation in water electrolysis and link these findings to previous measurements of electroconvective phenomena on IEMs. The measured characteristic times differ between the two systems only at large current densities ($i > i_R$), owing to the bulk chemical reaction for water equilibrium. Our estimates suggest that buoyancy plays a role in the present system, especially at the lower current densities. However, density-driven convection is not likely to influence the deviating trends of the transition times observed for larger i . We further present current and voltage measurements and compare them with estimates from simple models. These results along with pattern images may prove useful as a benchmark for future modeling and simulation efforts of electroconvection in electrolytic systems. Finally, we also reveal pattern formation up to a supporting electrolyte concentration $c_{\text{sup}} = 1$ mM, that is, for $c_{\text{sup}}/c_{\text{H}^+} \leq 0.5$ (see Appendix C).

Although electroconvection is unlikely in commercial electrolyzers (where excess supporting electrolyte is used), these findings are relevant to laboratory electrochemical studies which are frequently performed in the absence of supporting electrolyte [55,56]. Moreover, electroconvection could be the possible driving mechanism for the “spontaneous convection” (different from buoyancy-driven convection) which is assumed by Amatore *et al.* to successfully fit experimentally measured currents [57]. Measurements similar to those presented in this paper, with charged fluorescent dyes, could help check for this possibility. Note that the relation of overlimiting currents to electroconvective phenomena shown in the present study is only valid for planar electrode geometries. For more practical electrode designs, such as porous electrodes, or membrane-electrode geometries (which may allow gas

exchange and have a large surface area), overlimiting currents could also be driven by the interaction of the surface charge of pore walls with the electric field (surface conduction and electro-osmotic flow [58]). This may especially be relevant when the catalyst layer is separate from the pores, where there might also be a concentration gradient along the pore length.

It is readily apparent from the present study that, in order to explain the current or voltage response of electrolytic cells, a complete understanding of the relevant ion-transport processes is needed. This includes recognizing the role of convective instabilities and nonlinear bulk reactions in electrolytic systems. Additional experimental measurements under well-controlled conditions, with simple geometry (e.g., imposed one-dimensional flow) and reduced number of interacting ions (e.g., in CO_2 reduction with and without a buffer electrolyte), would certainly help establish to what extent transport processes affect the potential drop in solution.

ACKNOWLEDGMENTS

This research received funding from The Netherlands Organization for Scientific Research (NWO) in the framework of the fund New Chemical Innovations, project ELECTROGAS (731.015.204), with financial support from Akzo Nobel Chemicals, Shell Global Solutions, Magneto Special Anodes (an Evoqua Brand), and Elson Technologies. We acknowledge The Netherlands Center for Multiscale Catalytic Energy Conversion (MCEC) and the Max Planck Center Twente for Complex Fluid Dynamics for financial support. D.L. also acknowledges financial support by an ERC-Advanced Grant.

APPENDIX A: COMPARISON OF MEASURED AND THEORETICAL LINEAR SWEEP VOLTAMMOGRAMS

To further understand the $i - \phi$ measurement, a comparison could be made with an analytic solution of current density for linear sweeps, for example, a linear sweep with fast, reversible electrode kinetics (i.e., obeying the Nernst equation) [32,43]. A plot of the analytical expressions usually reveals a transient peak in the current density at the potentials at which the electrode reaction reaches diffusion limitation [32,43]. This is similar to the first green marker in Fig. 1(b). Following this peak, the theoretical curve decreases and approximately follows the Cottrell equation, that is, approaching i_{lim} [59]. We consider one such analytical expression, the modified Randles-Sevcik equation obtained by Yan *et al.* [43] (Eq. 33 there) which is valid for fast reactions (Nernst equation valid at the electrode boundary) in a fully supported electrolyte (no potential drop in the electrolyte). It therefore involves solving the semi-infinite diffusion equation for a single reacting ion. Note, however, that such an estimate cannot directly be

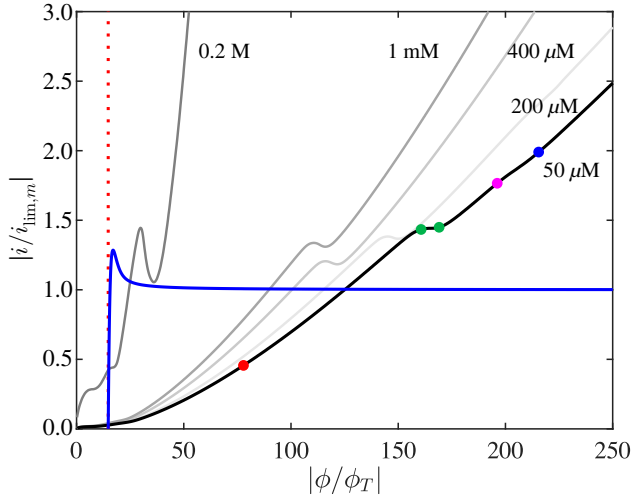


FIG. 7. Representative plot showing the normalized linear sweep voltammogram measured for different mentioned supporting electrolyte concentration for scan rate $v = 0.1$ V/s. The blue line is the analytical estimate and is based on the modified Randles-Sevcik equation (Eq. 33 in [43]), applicable for fast reactions in a fully supported solution (infinite supporting electrolyte) involving only one ionic species. Here $\phi = \phi_{\text{rev}}$ is taken as the x ordinate of the estimate and is given here by the red dotted line.

compared with the $i - \phi$ measurement in Fig. 1(b) (black line). As the analytical estimate neglects any potential drop in the bulk solution, in contrast to the experimental measurement (for the same potential sweep rate), it reaches the potential of diffusion limitation (the potential at which $c_{\text{H}^+} = 0$ at the electrode) much sooner. The thickness of the diffusion layer which goes as $\sqrt{D_{\text{H}^+}t}$ is therefore much smaller, and the predicted current density much larger than the experiment.

We scale out these differences in current densities by normalizing the analytical estimate and measurement with their respective Cottrell-like relationships. This result is presented in Fig. 7 where the primary measurement (black line) is compared with the analytical estimate (blue line). We also include results of linear sweep measurements done in solutions with different quantities of supporting electrolyte. Specifically, each i is normalized with a Cottrell-like current density $i_{\text{lim},m}$:

$$i_{\text{lim},m}(t) = -FD_{11} \frac{c_0}{(1 - \tau_{\text{H},m})\sqrt{\pi D_{11}t}}. \quad (\text{A1})$$

Equation (A1) is the modified limiting current density, $i_{\text{lim},m}$, which is a semiempirical extension of Eq. (1) for different supporting electrolyte concentrations [39]. The modified diffusion coefficient, D_{11} , and modified ion-transport number $\tau_{\text{H},m}$ are given by [39]

$$D_{11} = D_{\text{H}^+} \left(1 - \frac{c_0(D_{\text{H}^+} - D_{\text{ClO}_4^-})}{c_0(D_{\text{H}^+} + D_{\text{ClO}_4^-}) + c_{\text{sup}}(D_{\text{Na}^+} + D_{\text{ClO}_4^-})} \right), \quad (\text{A2a})$$

$$\tau_{\text{H},m} = \frac{c_0 D_{\text{H}^+}}{(c_0 D_{\text{H}^+} + (c_{\text{sup}} + c_0) D_{\text{ClO}_4^-} + c_{\text{sup}} D_{\text{Na}^+})}. \quad (\text{A2b})$$

Note that for $c_{\text{sup}} \gg c_0$, $D_{11} = D_{\text{H}^+}$ and $\tau_{\text{H},m} = 0$ and Eq. (A1) reduces to the usual form of the Cottrell equation [32]. For the other extreme case of a binary electrolyte, when $c_{\text{sup}} \ll c_0$, $D_{11} = D_S$ and $\tau_{\text{H},m} = \tau_{\text{H}^+}$, we obtain Eq. (1). Thus, normalizing with the modified Cottrell equation allows a better comparison between the $i - \phi$ relationships for all supporting electrolyte concentrations, because it helps scale out the differences in bulk ion transport.

It is apparent from Fig. 7 that for all supporting electrolyte concentrations, there is a transient peak associated with the fast linear sweep. There is also a clear trend: for the lower conductivity solutions, a larger potential is required to achieve diffusion limitation, likely because of greater electrical resistance of the electrolyte. The analytical result, valid for purely diffusive transport, further shows that i decreases to the diffusion limited value $i_{\text{lim},m}$ soon after the peak current. Comparing this curve with the experimental measurements, it can be seen that overlimiting currents are driven in all cases beyond a point. For a binary electrolyte (here $c_{\text{sup}} = 50 \mu\text{M}$) the overlimiting current is associated with pattern formation and electroconvection, as shown in the main text. With increasing c_{sup} , pattern formation (and likely electroconvection) is observed much later, and not at all for $c_{\text{sup}} = 0.2$ M. In these scenarios it is likely that buoyancy-driven mixing (owing to gradients in the concentration of the supporting electrolyte), supports the overlimiting current transport in the bulk electrolyte.

It should be noted that in the main text Eq. (1) is applied from the time when $|\phi| > |\phi_{\text{rev}}|$. This is not the case when calculating $i_{\text{lim},m}$ for the measured curves here. The time $t = 0$ in $i_{\text{lim},m}$ for the experimental measurements corresponds to $|\phi| = 0$ V vs Ag/AgCl (and not $\phi = \phi_{\text{rev}} = 0.3972$ V) (this is done so that i values at $\phi < \phi_{\text{rev}}$ are also normalized). In contrast, the analytical expression (and corresponding $i_{\text{lim},m}$) only begins at $\phi = \phi_{\text{rev}}$. This, however, does not change the discussion and conclusion drawn in the preceding paragraphs.

APPENDIX B: NUMERICAL MODEL

A simplified numerical model is derived here, primarily to calculate Sand's time for the present system.

The general form of the Nernst-Planck-Poisson equations with a bulk reaction is

$$\frac{\partial c_k}{\partial t} = \frac{\partial J_k}{\partial z} + R_k, \quad (\text{B1a})$$

$$J_k = D_k \left(\frac{\partial c_k}{\partial z} + \frac{z_k F c_k}{RT} \frac{\partial \phi}{\partial z} \right), \quad (\text{B1b})$$

$$\varepsilon \nabla^2 \phi = - \sum_{k=1}^n Z_k F c_k, \quad (\text{B1c})$$

where c_k is the concentration, J_k is the mass flux, and Z_k is the sign of the charge of k th ionic species, for a total “ n ” number of ions. Here R_k is the bulk reaction for each equation, ϕ is the electrostatic potential in solution, and ε is the absolute permittivity of water. More specifically, taking an acid with anion ClO_4^- and a supporting salt with cation Na^+ and anion ClO_4^- , we have

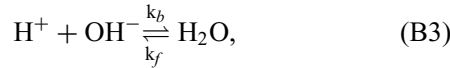
$$\frac{\partial c_{\text{H}^+}}{\partial t} = D_{\text{H}^+} \frac{\partial}{\partial z} \left(\frac{\partial c_{\text{H}^+}}{\partial z} + \frac{F c_{\text{H}^+}}{RT} \frac{\partial \phi}{\partial z} \right) + R, \quad (\text{B2a})$$

$$\frac{\partial c_{\text{ClO}_4^-}}{\partial t} = D_{\text{ClO}_4^-} \frac{\partial}{\partial z} \left(\frac{\partial c_{\text{ClO}_4^-}}{\partial z} - \frac{F c_{\text{ClO}_4^-}}{RT} \frac{\partial \phi}{\partial z} \right), \quad (\text{B2b})$$

$$\frac{\partial c_{\text{OH}^-}}{\partial t} = D_{\text{OH}^-} \frac{\partial}{\partial z} \left(\frac{\partial c_{\text{OH}^-}}{\partial z} - \frac{F c_{\text{OH}^-}}{RT} \frac{\partial \phi}{\partial z} \right) + R, \quad (\text{B2c})$$

$$\frac{\partial c_{\text{Na}^+}}{\partial t} = D_{\text{Na}^+} \frac{\partial}{\partial z} \left(\frac{\partial c_{\text{Na}^+}}{\partial z} + \frac{F c_{\text{Na}^+}}{RT} \frac{\partial \phi}{\partial z} \right). \quad (\text{B2d})$$

Here, $R = k_b c_W - k_f c_{\text{H}^+} c_{\text{OH}^-}$ is the bulk dissociation of water for the reaction,



where $k_b = 2.6 \times 10^{-5} \text{ s}^{-1}$ is the water dissociation rate constant and $k_f = 1.4 \times 10^{11} \text{ M}^{-1} \text{ s}^{-1}$ is the rate constant for H^+ and OH^- association [60]. Note that the concentration of water, $c_W = 55.55 \text{ M}$, is assumed to be constant (and much larger than the H^+ or OH^- concentration).

1. (Acidic) binary electrolyte (acid)

Assuming electroneutrality, we get continuity of the current, that is, the current (or charge flux) is constant in the system and equal to the value at the boundary. In other words,

$$\begin{aligned} \Sigma Z_k J_k &= \frac{\partial}{\partial z} \left(D_{\text{H}^+} c_{\text{H}^+} - D_{\text{ClO}_4^-} c_{\text{ClO}_4^-} \right. \\ &\quad \left. - D_{\text{OH}^-} c_{\text{OH}^-} + D_{\text{Na}^+} c_{\text{Na}^+} \right) \\ &\quad + \frac{F}{RT} \frac{\partial \phi}{\partial z} \left(D_{\text{H}^+} c_{\text{H}^+} + D_{\text{ClO}_4^-} c_{\text{ClO}_4^-} \right. \\ &\quad \left. + D_{\text{OH}^-} c_{\text{OH}^-} + D_{\text{Na}^+} c_{\text{Na}^+} \right) = \frac{i}{F}. \end{aligned} \quad (\text{B4})$$

As electroneutrality implies that $c_{\text{H}^+} + c_{\text{Na}^+} = c_{\text{ClO}_4^-} + c_{\text{OH}^-} = c$, the previous equations can be rewritten as

$$\begin{aligned} &\frac{\partial}{\partial z} \left((D_{\text{H}^+} - D_{\text{OH}^-})c - (D_{\text{H}^+} - D_{\text{Na}^+})c_{\text{Na}^+} \right. \\ &\quad \left. + (D_{\text{OH}^-} - D_{\text{ClO}_4^-})c_{\text{ClO}_4^-} \right) \\ &\quad + \frac{F}{RT} \frac{\partial \phi}{\partial z} \left((D_{\text{H}^+} + D_{\text{OH}^-})c - (D_{\text{H}^+} - D_{\text{Na}^+})c_{\text{Na}^+} \right. \\ &\quad \left. - (D_{\text{OH}^-} - D_{\text{ClO}_4^-})c_{\text{ClO}_4^-} \right) = \frac{i}{F}. \end{aligned} \quad (\text{B5})$$

Consider the case where $c_{\text{Na}^+}, c_{\text{OH}^-} \ll c_{\text{H}^+} = c_{\text{ClO}_4^-} = c$, that is, the (initial) concentration of OH^- is very small and there is close to no supporting electrolyte in solution. The gradient in the potential in this case is given by

$$\frac{\partial \phi}{\partial z} = \frac{RT}{Fc} \frac{1}{(D_{\text{H}^+} + D_{\text{ClO}_4^-})} \left(\frac{i}{F} - (D_{\text{H}^+} - D_{\text{ClO}_4^-}) \frac{\partial c}{\partial z} \right). \quad (\text{B6})$$

Furthermore, note that in Eq. (B2) the contribution of the potential gradient term is of the form

$$\begin{aligned} &D_k \frac{\partial}{\partial z} \left(c_k \frac{\partial \phi}{\partial z} \right) \\ &= D_k \frac{\partial}{\partial z} \left(\frac{c_k}{c} \frac{RT}{F(D_{\text{H}^+} + D_{\text{ClO}_4^-})} (i - (D_{\text{H}^+} - D_{\text{ClO}_4^-}) \frac{\partial c}{\partial z}) \right). \end{aligned} \quad (\text{B7})$$

As $c_{\text{OH}^-}/c \sim c_{\text{Na}^+}/c \sim 0$, the contribution of the potential gradient term to the transport of OH^- and the salt cation is negligible. Equations (B2c) and (B2d) can now be written as

$$\frac{\partial c_{\text{OH}^-}}{\partial t} = D_{\text{OH}^-} \frac{\partial}{\partial z} \left(\frac{\partial c_{\text{OH}^-}}{\partial z} \right) + R, \quad (\text{B8a})$$

$$\frac{\partial c_{\text{Na}^+}}{\partial t} = D_{\text{Na}^+} \frac{\partial}{\partial z} \left(\frac{\partial c_{\text{Na}^+}}{\partial z} \right), \quad (\text{B8b})$$

with the boundary conditions

$$c_k \Big|_{z \rightarrow \infty} = c_{k,\text{initial}} \quad (\text{B9})$$

and

$$D_{\text{OH}^-} \left(\frac{\partial c_{\text{OH}^-}}{\partial z} \right) \Big|_{z=0} = 0, \quad (\text{B10a})$$

$$D_{\text{Na}^+} \left(\frac{\partial c_{\text{Na}^+}}{\partial z} \right) \Big|_{z=0} = 0. \quad (\text{B10b})$$

In addition, Eqs. (B2a) and (B2b) and the related boundary conditions

$$D_{\text{H}^+} \left(\frac{\partial c}{\partial z} + \frac{Fc}{RT} \frac{\partial \phi}{\partial z} \right) \Big|_{z=0} = \frac{i}{F}, \quad (\text{B11a})$$

$$D_{\text{ClO}_4^-} \left(\frac{\partial c}{\partial z} - \frac{Fc}{RT} \frac{\partial \phi}{\partial z} \right) \Big|_{z=0} = 0, \quad (\text{B11b})$$

can further be reduced to the diffusion equation, with the additional reaction term, for an effective salt species c_S , following the procedure for a binary electrolyte by [39,61].

The final set of equations that are solved are

$$\frac{\partial c_S}{\partial t} = D_S \frac{\partial^2 c}{\partial z^2} + \frac{D_{\text{ClO}_4^-}}{D_{\text{H}^+} + D_{\text{ClO}_4^-}} R \quad (\text{B12a})$$

$$\frac{\partial c_{\text{OH}^-}}{\partial t} = D_{\text{OH}^-} \frac{\partial^2 c_{\text{OH}^-}}{\partial z^2} + R \quad (\text{B12b})$$

with boundary conditions

$$c_S \Big|_{z=l} = c_0, \quad (\text{B13a})$$

$$c_{\text{OH}^-} \Big|_{z=l} = \frac{k_b c_W}{k_f c_0}, \quad (\text{B13b})$$

and

$$\frac{D_S}{1 - t_{\text{H}}} \frac{\partial c_S}{\partial z} \Big|_{z=0} = \frac{i}{F}, \quad (\text{B14a})$$

$$D_{\text{OH}^-} \left(\frac{\partial c_{\text{OH}^-}}{\partial z} \right) \Big|_{z=0} = 0, \quad (\text{B14b})$$

where $D_S = 2D_{\text{H}^+}D_{\text{ClO}_4^-}/(D_{\text{H}^+} + D_{\text{ClO}_4^-})$ and $\tau_{\text{H}^+} = D_{\text{H}^+}/(D_{\text{H}^+} + D_{\text{ClO}_4^-})$.

2. Excess supporting electrolyte (supp)

We can also derive a simplified model for ion transport for the case when the electrolyte solution contains excess supporting electrolyte. Although not directly applicable to the present experimental system, it helps provide a lower limit for the measured transition times. Here, in addition to assuming electroneutrality, we also have $c_{\text{H}^+}, c_{\text{OH}^-} \ll$

$c_{\text{Na}^+} = c_{\text{ClO}_4^-} = c$. Similarly, the potential gradient is given by

$$\frac{\partial \phi}{\partial z} = \frac{RT}{Fc} \frac{1}{(D_{\text{Na}^+} + D_{\text{ClO}_4^-})} \left(\frac{i}{F} - (D_{\text{Na}^+} - D_{\text{ClO}_4^-}) \frac{\partial c}{\partial z} \right). \quad (\text{B15})$$

Here, instead, $c_{\text{OH}^-}/c \sim c_{\text{H}^+}/c \sim 0$ and the contribution of the potential-gradient term to the transport of H^+ and OH^- is negligible. The equations reduce to a reaction-diffusion system

$$\frac{\partial c_{\text{H}^+}}{\partial t} = D_{\text{H}^+} \frac{\partial^2 c_{\text{H}^+}}{\partial z^2} + R, \quad (\text{B16a})$$

$$\frac{\partial c_{\text{OH}^-}}{\partial t} = D_{\text{OH}^-} \frac{\partial^2 c_{\text{OH}^-}}{\partial z^2} + R, \quad (\text{B16b})$$

with boundary conditions

$$c_{\text{H}^+}(l) = c_0, \quad (\text{B17a})$$

$$c_{\text{OH}^-}(l) = \frac{k_b c_W}{k_f c_0} \quad (\text{B17b})$$

at $z = l$ (where c_0 is the initial H^+ concentration) and

$$\frac{\partial c_{\text{H}^+}}{\partial z} = \frac{i_F}{D_{\text{H}^+} F}, \quad (\text{B18a})$$

$$\frac{\partial c_{\text{OH}^-}}{\partial z} = 0, \quad (\text{B18b})$$

at the electrode surface. Note that in this case the potential gradient in solution is obtained by solving the transport equations for the supporting electrolyte.

We use a second-order finite-difference approximation with the implicit integration factor (IIF) numerical scheme presented by Nie *et al.* [65] to solve the reaction-diffusion models given previously (as done in our recent work [20]). For the calculation, we use a time resolution of $\Delta t = 0.03$ s and a spatial resolution of $\Delta z = 10$ μm for the calculations. Values of the constants used are presented in Table II. The corresponding Sand's time for the above two models, t_{acid} and t_{supp} , is the time when the concentration of the reacting ion $c = 0$ at the boundary.

3. Estimating potential drop in the double layer

For the chronopotentiometric experiments, the measured potential ϕ_{exp} is the total potential drop between the working and the reference electrode, i.e., $\phi_{\text{exp}} = \Delta\phi_S + \Delta\phi_D + \Delta\phi_{\text{bulk}}$, where $\Delta\phi_S$ and $\Delta\phi_D$ are the potential drop in Stern and diffuse layer, respectively, and $\Delta\phi_{\text{bulk}}$ is the potential drop in the bulk electroneutral solution. Here $\Delta\phi_S$ is the potential difference that drives the reaction and is assumed to be equal to the reversible potential

TABLE II. Values of the used constants.

| | |
|--|---|
| $D_{\text{H}^+} = 9.3 \times 10^{-9} \text{ m}^2/\text{s}$ [62] | $D_{\text{OH}^-} = 4.5 \times 10^{-9} \text{ m}^2/\text{s}$ [63] |
| $k_b = 2.6 \times 10^{-5} \text{ s}^{-1}$ [60] | $k_f = 1.4 \times 10^{11} \text{ s}^{-1} \text{ M}^{-1}$ [60] |
| $D_{\text{ClO}_4^-} =$ $1.792 \times 10^{-9} \text{ m}^2/\text{s}$ [64] | $c_W = 55.55 \text{ M}$ |

for hydrogen evolution (0 V vs RHE). Measured on the Ag/AgCl reference electrode scale, this value is $\phi_{\text{rev}} = 0 - 0.059 \text{ pH} - \phi_{\text{Ag/AgCl}}^0 = -0.3792 \text{ V}$ where $\phi_{\text{Ag/AgCl}}^0 = 0.22 \text{ V}$ (at 298 K) is the standard potential for the reference electrode [66]. Furthermore, the results of the numerical model “acid” can be used to calculate $\Delta\phi_{\text{bulk}}$ by integrating Eq. (B6). This combined numerical value $\Delta\phi_{\text{sim}} = \Delta\phi_{\text{bulk}} + \phi_{\text{rev}}$ is presented along with the ϕ_{exp} in Figs. 8(a)–8(f) for increasing $|i|$, respectively. The difference is an estimate of $\Delta\phi_D$, where for all current densities $\Delta\phi_D > 1 \text{ V}$. This implies that within the Debye layer, which has a thickness of $\lambda_D = 6.8 \text{ nm}$, the electric field strength $E_D \approx 1/\lambda_D \text{ V/m} = 1 \text{ MV/cm}$. This is sufficiently large to increase the dissociation rate of water [35,36] beyond its bulk value k_b . For $E_D = 1 \text{ MV/cm}$ the increased dissociation constant is calculated to be approximately equal to $3k_b$ [using Eq. (38) in [36]]. Thus, the water dissociation rate is at least three times as fast in the double layer than in the bulk solution and can plausibly contribute additional protons for the reaction at the electrode.

APPENDIX C: PATTERNS AT DIFFERENT SUPPORTING ELECTROLYTE CONCENTRATIONS

In Fig. 9 we show additional images of patterns at onset (visual inspection), at different supporting salt concentrations (here NaClO_4 ; c_{sup}), for the highest current

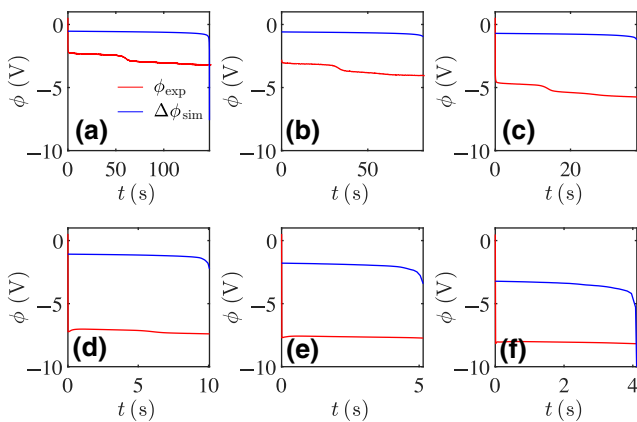


FIG. 8. The measured electrode potential ϕ_{exp} compared with that calculated from the electroneutral numerical model $\Delta\phi_{\text{sim}}$. The difference indicates the potential drop in the Debye layer.

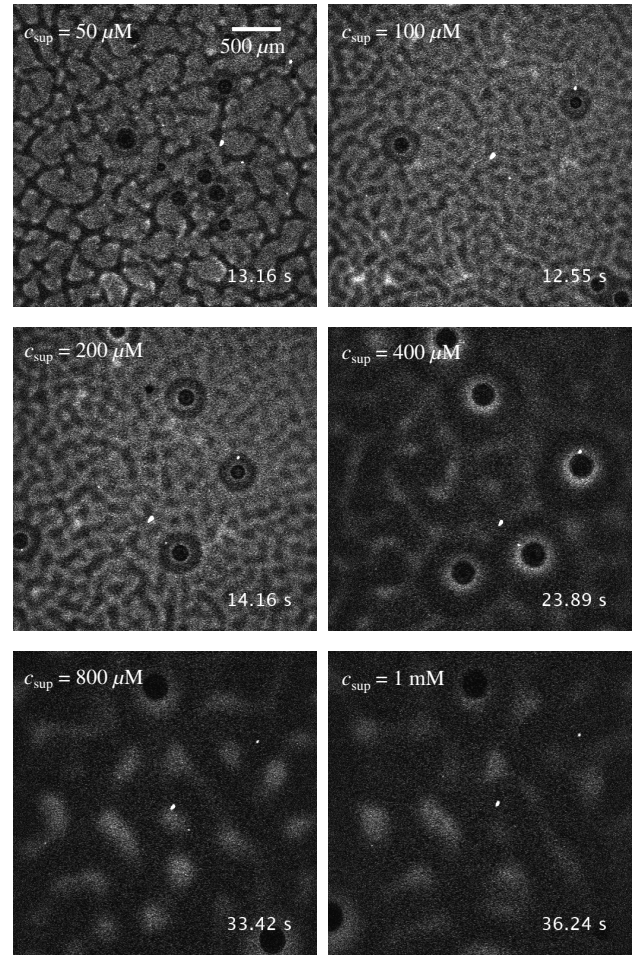


FIG. 9. Patterns formed for different supporting electrolyte concentration (shown in the upper left corner) for $|i| = 7.96 \text{ mA/cm}^2$ at their onset. The time of onset of the pattern, after the current is applied, is shown in the bottom right corner.

density considered in our work $i = 7.96 \text{ mA/cm}^2$ ($i \approx 5i_R$). In each case, $c_{\text{Na}^+} < c_{\text{H}^+}$. The images show the pattern at the moment of onset, and the time of onset is mentioned in the right bottom corner of the image. A general observation is that with increasing supporting electrolyte concentration, c_{sup} , the onset time of the pattern as well as the initial wavelength of the pattern (wavelength of fluorescence intensity variation) increases. There appears to be, in fact, a sudden increase in initial pattern wavelength between $200 \mu\text{M} < c_{\text{sup}} < 400 \mu\text{M}$.

APPENDIX D: PATTERN IMAGES FOR ALL CURRENT DENSITIES

In Fig. 10 we present the images of the pattern at equal intervals (10 s) after their onset $t_{\text{EKI}} \approx t_{\text{ons}}$. The pattern images for almost all the current densities appear to grow in a similar manner as shown quantitatively in Fig. 2 in the main text. For the lowest current density, however,

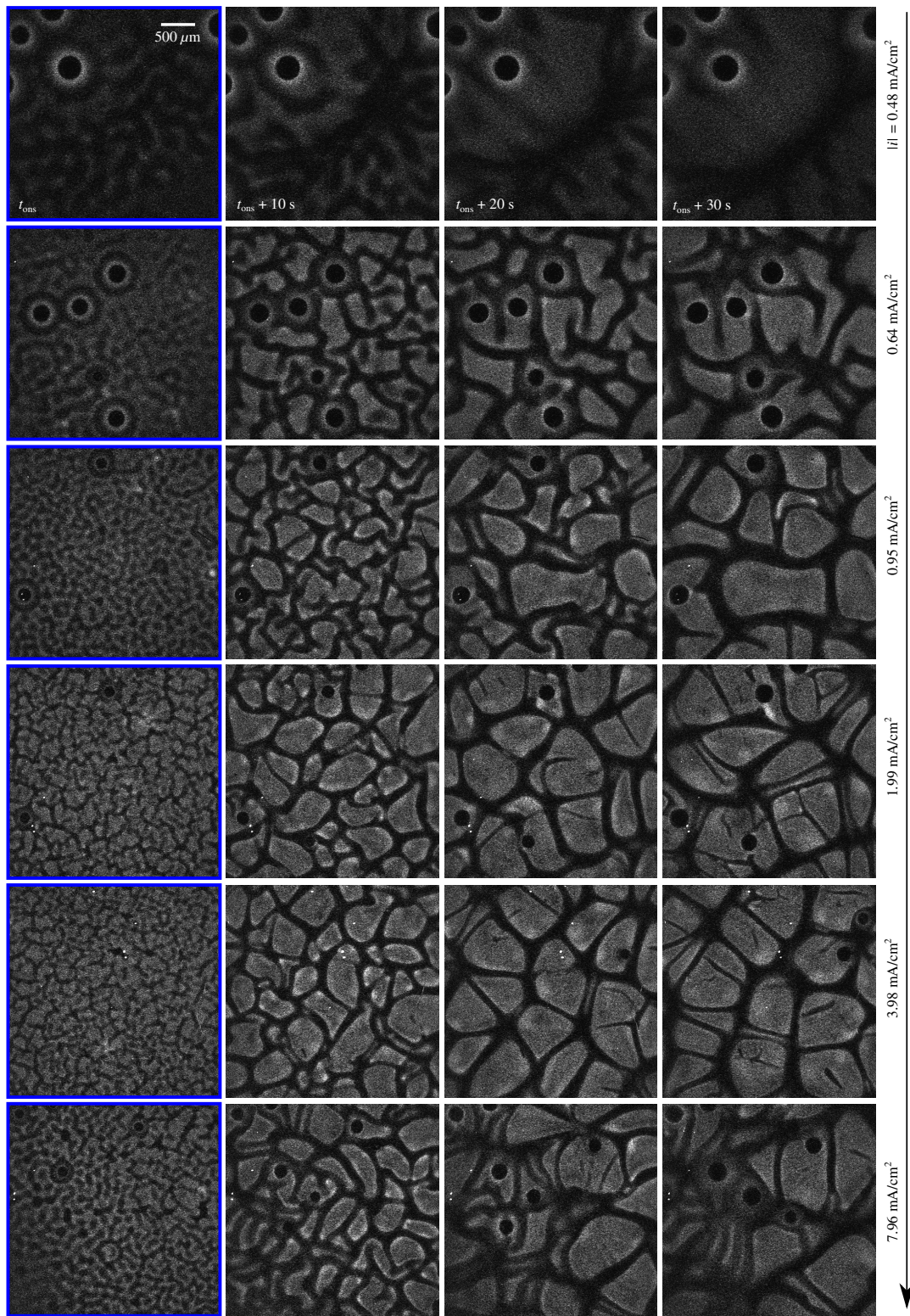


FIG. 10. Patterns formed for different applied currents at approximately 10 s intervals after onset t_{ons} .

the smoothing of the pattern could be brought about by large-scale buoyant convection.

-
- [1] Z. Yan, J. L. Hitt, J. A. Turner, and T. E. Mallouk, Renewable electricity storage using electrolysis, *Proc. Natl. Acad. Sci. U.S.A.* **117**, 12558 (2020).
- [2] R. L. LeRoy, Industrial water electrolysis: Present and future, *Int. J. Hydrog. Energy* **8**, 401 (1983).
- [3] T. Burdyny and W. A. Smith, CO₂ reduction on gas-diffusion electrodes and why catalytic performance must be assessed at commercially-relevant conditions, *Energy Environ. Sci.* **12**, 1442 (2019).
- [4] C. Wagner, The role of natural convection in electrolytic processes, *J. Electrochem. Soc.* **95**, 161 (1949).
- [5] K. Ngamchuea, S. Eloul, K. Tschulik, and R. G. Compton, Advancing from rules of thumb: Quantifying the effects of small density changes in mass transport to electrodes. Understanding natural convection, *Anal. Chem.* **87**, 7226 (2015).
- [6] I. Rubinstein and B. Zaltzman, Electro-osmotically induced convection at a permselective membrane, *Phys. Rev. E* **62**, 2238 (2000).
- [7] C. Druzgalski and A. Mani, Statistical analysis of electroconvection near an ion-selective membrane in the highly chaotic regime, *Phys. Rev. Fluids* **1**, 073601 (2016).
- [8] A. Mani and K. M. Wang, Electroconvection near electrochemical interfaces: Experiments, *Mod. Comput., Annu. Rev. Fluid Mech.* **52**, 509 (2020).
- [9] S. M. Rubinstein, G. Manukyan, A. Staicu, I. Rubinstein, B. Zaltzman, R. G. H. Lammertink, F. Mugele, and M. Wessling, Direct Observation of a Nonequilibrium Electro-Osmotic Instability, *Phys. Rev. Lett.* **101**, 236101 (2008).
- [10] G. Yossifon and H.-C. Chang, Selection of Nonequilibrium Overlimiting Currents: Universal Depletion Layer Formation Dynamics and Vortex Instability, *Phys. Rev. Lett.* **101**, 254501 (2008).
- [11] S. Kang and R. Kwak, Pattern Formation of Three-Dimensional Electroconvection on a Charge Selective Surface, *Phys. Rev. Lett.* **124**, 154502 (2020).
- [12] V. V. Nikonenko, A. V. Kovalenko, M. K. Urtenov, N. D. Pismenskaya, J. Han, P. Sistat, and G. Pourcelly, Desalination at overlimiting currents: State-of-the-art and perspectives, *Desalination* **342**, 85 (2014).
- [13] V. Fleury, J.-N. Chazalviel, and M. Rosso, Theory and Experimental Evidence of Electroconvection around Electrochemical Deposits, *Phys. Rev. Lett.* **68**, 2492 (1992).
- [14] V. Fleury, J. N. Chazalviel, and M. Rosso, Coupling of drift, diffusion, and electroconvection, in the vicinity of growing electrodeposits, *Phys. Rev. E* **48**, 1279 (1993).
- [15] J. M. Huth, H. L. Swinney, W. D. McCormick, A. Kuhn, and F. Argoul, Role of convection in thin-layer electrodeposition, *Phys. Rev. E* **51**, 3444 (1995).
- [16] P. Bai, J. Li, F. R. Brushett, and M. Z. Bazant, Transition of lithium growth mechanisms in liquid electrolytes, *Energy Environ. Sci.* **9**, 3221 (2016).
- [17] D. Zhang, A. J. Warren, G. Li, Z. Cheng, X. Han, Q. Zhao, X. Liu, Y. Deng, and L. A. Archer, Electrodeposition of zinc in aqueous electrolytes containing high molecular weight polymers, *Macromolecules* **53**, 2694 (2020).
- [18] J. Kim, S. Davidson, and A. Mani, Characterization of chaotic electroconvection near flat inert electrodes under oscillatory voltages, *Micromachines* **10**, 1 (2019).
- [19] M. B. Andersen, D. M. Rogers, J. Mai, B. Schudel, A. V. Hatch, S. B. Rempe, and A. Mani, Spatiotemporal pH dynamics in concentration polarization near ion-selective membranes, *Langmuir* **30**, 7902 (2014).
- [20] N. Pande, S. K. Chandrasekar, D. Lohse, G. Mul, J. A. Wood, B. T. Mei, and D. Krug, Electrochemically induced pH change: Time-resolved confocal fluorescence microscopy measurements and comparison with numerical model, *J. Phys. Chem. Lett.* **11**, 7042 (2020).
- [21] K. Obata, R. van de Krol, M. Schwarze, R. Schomäcker, and F. Abdi, In-situ observation of pH change during water splitting in neutral pH conditions: Impact of natural convection driven by buoyancy effects, *Energy Environ. Sci.* **10**, 147 (2020).
- [22] A. De Wit, Chemo-hydrodynamic patterns and instabilities, *Ann. Rev. Fluid. Mech.* **52**, 531 (2020).
- [23] H. Köstlin and H. Schaper, Electrochemiluminescence by dc of rubrene displaying highly organized electrohydrodynamic convection, *Phys. Lett. A* **76**, 455 (1980).
- [24] M. Orlik, J. Rosenmund, K. Doblhofer, and G. Ertl, Electrochemical formation of luminescent convective patterns in thin-layer cells, *J. Phys. Chem. B* **102**, 1397 (1998).
- [25] M. Orlik, K. Doblhofer, and G. Ertl, On the mechanism of electrohydrodynamic convection in thin-layer electrolytic cells, *J. Phys. Chem. B* **102**, 6367 (1998).
- [26] S. Sato and M. Sano, Nonlinear pattern formation by electroconvection of carbon nanotube dispersions, *Langmuir* **23**, 10984 (2007).
- [27] Y. Han and D. G. Grier, Colloidal electroconvection in a thin horizontal cell. II. Bulk electroconvection of water during parallel-plate electrolysis, *J. Chem. Phys.* **125**, 144707 (2006).
- [28] Here, the counter electrode (also diameter $\sigma = 4$ cm) is a ring electrode (radial symmetry; and a thickness of approximately 1 mm), and is placed 4 cm away from the working electrode. This distance is much larger than the diffusion length scale of the system for $\sqrt{D_{St}} \sim 3$ mm. We therefore expect no influence of the counter electrode on our results.
- [29] J. Coppeta and C. Rogers, Dual emission laser induced fluorescence for direct planar scalar behavior measurements, *Exp. Fluids* **25**, 1 (1998).
- [30] K. Scida, A. Eden, N. Arroyo-Currás, S. MacKenzie, Y. Satik, C. D. Meinhart, J. C. T. Eijkel, and S. Penathur, Fluorescence-based observation of transient electrochemical and electrokinetic effects at nanoconfined bipolar electrodes, *ACS Appl. Mater. Interfaces* **11**, 13777 (2019).
- [31] I. Rubinstein and L. Shtilman, Voltage against current curves of cation exchange membranes, *J. Chem Soc., Faraday Trans. 2* **75**, 231 (1979).
- [32] A. J. Bard and L. R. Faulkner, *Electrochemical Methods: Fundamentals and Applications* (Wiley, New York, 2002), Vol. 38, 2nd ed.
- [33] Y. Yaguchi, M. Tachikawa, Z. Zhang, and T. Terasaki, Organic anion-transporting polypeptide 1a4 (Oatp1a4/

- Scol1a4) at the blood-arachnoid barrier is the major pathway of sulforhodamine-101 clearance from cerebrospinal fluid of rats, *Mol. Pharm.* **16**, 2021 (2019).
- [34] S. M. Davidson, M. Wessling, and A. Mani, On the dynamical regimes of pattern-accelerated electroconvection, *Sci. Rep.* **6**, 1 (2016).
- [35] L. Onsager, Deviations from ohm's law in weak electrolytes, *J. Chem. Phys.* **2**, 599 (1934).
- [36] Y. Tanaka, Water dissociation reaction generated in an ion exchange membrane, *J. Mem. Sci.* **350**, 347 (2010).
- [37] J. C. de Valença, R. M. Wagterveld, R. G. H. Lammertink, and P. A. Tsai, Dynamics of microvortices induced by ion concentration polarization, *Phys. Rev. E* **92**, 031003 (2015).
- [38] J. C. de Valença, A. Kurniawan, R. M. Wagterveld, J. A. Wood, and R. G. H. Lammertink, Influence of Rayleigh-Bénard convection on electrokinetic instability in overlimiting current conditions, *Phys. Rev. Fluids* **2**, 033701(R) (2017).
- [39] M. D. Morris and J. J. Lingane, The effect of electrical migration on the chronopotentiometric transition time, *J. Electroanal. Chem.* **6**, 300 (1963).
- [40] A. Bonnefont, F. Argoul, and M. Z. Bazant, Asymptotic analysis of diffuse-layer effects on time-dependent interfacial kinetics, *J. Electroanal. Chem.* **500**, 52 (2000).
- [41] M. van Soestbergen, P. M. Biesheuvel, and M. Z. Bazant, Diffuse-charge effects on the transient response of electrochemical cells, *Phys. Rev. E* **81**, 021503 (2010).
- [42] M. Van Soestbergen, Frumkin-Butler-Volmer theory and mass transfer in electrochemical cells, *Russ. J. Electrochem.* **48**, 570 (2012).
- [43] D. Yan, M. Z. Bazant, P. M. Biesheuvel, M. C. Pugh, and F. P. Dawson, Theory of linear sweep voltammetry with diffuse charge: Unsupported electrolytes, thin films, and leaky membranes, *Phys. Rev. E* **95**, 033303 (2017).
- [44] K. C. Neyerlin, W. Gu, J. Jorne, and H. A. Gasteiger, Study of the exchange current density for the hydrogen oxidation and evolution reactions, *J. Electrochem. Soc.* **154**, B631 (2007).
- [45] B. Conway and B. Tilak, Interfacial processes involving electrocatalytic evolution and oxidation of H₂, and the role of chemisorbed H, *Electrochim. Acta* **47**, 3571 (2002).
- [46] I. Streeter and R. G. Compton, Numerical simulation of potential step chronoamperometry at low concentrations of supporting electrolyte, *J. Phys. Chem. C* **112**, 13716 (2008).
- [47] E. J. Dickinson and R. G. Compton, The zero-field approximation for weakly supported voltammetry: A critical evaluation, *Chem. Phys. Lett.* **497**, 178 (2010).
- [48] E. Karatay, M. B. Andersen, M. Wessling, and A. Mani, Coupling between Buoyancy Forces and Electroconvective Instability near Ion-Selective Surfaces, *Phys. Rev. Lett.* **116**, 194501 (2016).
- [49] L. H. Brickwedde, Properties of aqueous solutions of perchloric acid, *J. Res. Natl. Bureau Stand.* **42**, 309 (1949).
- [50] E. M. Sparrow, R. J. Goldstein, and V. K. Jonsson, Thermal instability in a horizontal fluid layer: Effect of boundary conditions and non-linear temperature profile, *J. Fluid Mech.* **18**, 513 (1964).
- [51] K. K. Tan and R. B. Thorpe, The onset of convection caused by buoyancy during transient heat conduction in deep fluids, *Chem. Eng. Sci.* **51**, 4127 (1996).
- [52] See Supplemental Material at <http://link.aps.org/supplemental/10.1103/PhysRevApplied.16.034021> for movie of particle motion and fluorescence patterns.
- [53] J. W. Swan and E. M. Furst, A simpler expression for Henry's function describing the electrophoretic mobility of spherical colloids, *J. Colloid Interface Sci.* **388**, 92 (2012).
- [54] O. Schnitzer and E. Yariv, Strong electro-osmotic flows about dielectric surfaces of zero surface charge, *Phys. Rev. E* **89**, 043005 (2014).
- [55] W. Sheng, H. A. Gasteiger, and Y. Shao-Horn, Hydrogen oxidation and evolution reaction kinetics on platinum: Acid vs alkaline electrolytes, *J. Electrochem. Soc.* **157**, B1529 (2010).
- [56] A. Bashkatov, S. S. Hossain, X. Yang, G. Mutschke, and K. Eckert, Oscillating Hydrogen Bubbles at Pt Microelectrodes, *Phys. Rev. Lett.* **123**, 214503 (2019).
- [57] C. Amatore, S. Szunerits, L. Thouin, and J.-S. Warkocz, The real meaning of Nernst's steady diffusion layer concept under non-forced hydrodynamic conditions. A simple model based on Levich's seminal view of convection, *J. Electroanal. Chem.* **500**, 62 (2001).
- [58] E. V. Dydek, B. Zaltzman, I. Rubinstein, D. S. Deng, A. Mani, and M. Z. Bazant, Overlimiting Current in a Microchannel, *Phys. Rev. Lett.* **107**, 1 (2011).
- [59] This result can be easily shown by plotting, for example, the modified Randles-Sevcik equation [43] (Eq. 33 there) alongside i_{lim} in Fig. 1(b). However, because it does not add substantially to the figure, this is avoided here.
- [60] F. H. Stillinger, Proton transfer reactions and kinetics in water, *Theor. Chem.: Adv. Perspect.* **3**, 177 (1978).
- [61] J. S. Newman and K. E. Thomas-Alyea, *Electrochemical Systems* (Wiley, New York, 2004), 3rd ed.
- [62] R. A. Robinson and R. H. Stokes, *Electrolyte Solutions* (Dover Publications, Dover, 2002).
- [63] S. Daniele, M. A. Baldo, C. Bragato, M. E. Abdelsalam, and G. Denuault, Steady-state voltammetry of hydroxide ion oxidation in aqueous solutions containing ammonia, *Anal. Chem.* **74**, 3290 (2002).
- [64] S. R. Heil, M. Holz, T. M. Kastner, and H. Weingärtner, Self-diffusion of the perchlorate ion in aqueous electrolyte solutions measured by ³⁵Cl NMR spin-echo experiments, *J. Chem. Soc., Faraday Trans.* **91**, 1877 (1995).
- [65] Q. Nie, Y.-T. Zhang, and R. Zhao, Efficient semi-implicit schemes for stiff systems, *J. Comp. Phys.* **214**, 521 (2006).
- [66] R. G. Bates and J. B. Macaskill, Standard potential of the silver-silver chloride electrode, *Pure Appl. Chem.* **50**, 1701 (1978).